

Calculating and communicating ensemble-based volcanic ash dosage and concentration risk for aviation

Article

Accepted Version

Prata, A. T., Dacre, H. F., Irvine, E. A., Mathieu, E., Shine, K. P. and Clarkson, R. J. (2019) Calculating and communicating ensemble-based volcanic ash dosage and concentration risk for aviation. *Meteorological Applications*, 26 (2). pp. 253-266. ISSN 1469-8080 doi: <https://doi.org/10.1002/met.1759>
Available at <http://centaur.reading.ac.uk/79259/>

It is advisable to refer to the publisher's version if you intend to cite from the work. See [Guidance on citing](#).

To link to this article DOI: <http://dx.doi.org/10.1002/met.1759>

Publisher: Royal Meteorological Society

All outputs in CentAUR are protected by Intellectual Property Rights law, including copyright law. Copyright and IPR is retained by the creators or other copyright holders. Terms and conditions for use of this material are defined in the [End User Agreement](#).

www.reading.ac.uk/centaur

CentAUR

Central Archive at the University of Reading

Reading's research outputs online

1

2 **Calculating and communicating ensemble-based volcanic**

3 **ash dosage and concentration risk for aviation**

4 Andrew T. Prata,^{a*} Helen F. Dacre,^a Emma A. Irvine,^a Eric Mathieu,^a Keith P. Shine^a and
5 Rory J. Clarkson^b

6 *^aDepartment of Meteorology, University of Reading, UK*

7 *^bEngine Environmental Protection, Rolls-Royce plc, Derby, UK*

8

9

10 **ABSTRACT:** During volcanic eruptions, aviation stakeholders require an assessment of the
11 volcanic ash hazard. Operators and regulators are required to make fast decisions based on
12 deterministic forecasts, which are subject to various sources of uncertainty. For a robust decision
13 to be made, a measure of the uncertainty of the hazard should be considered but this can lead to
14 added complexity preventing fast decision making. Here a proof-of-concept risk matrix approach
15 is presented that combines uncertainty estimation and volcanic ash hazard forecasting into a
16 simple warning system for aviation. To demonstrate the methodology, an ensemble of 600
17 dispersion model simulations is used to characterise uncertainty (due to eruption source
18 parameters, meteorology and internal model parameters) in ash dosages and concentrations for a
19 hypothetical Icelandic eruption. To simulate aircraft encounters with volcanic ash, trans-Atlantic
20 air routes between New York (JFK) and London (LHR) are generated using time-optimal routing
21 software. This approach has been developed in collaboration with operators, regulators and
22 engine manufacturers; it demonstrates how an assessment of ash dosage and concentration risk

23 can be used to make fast and robust flight-planning decisions even when the model uncertainty
24 spans several orders of magnitude. The results highlight the benefit of using an ensemble over a
25 deterministic forecast and a new method for visualising dosage risk along flight paths. The risk
26 matrix approach is applicable to other aviation hazards such as SO₂ dosages, desert dust, aircraft
27 icing and clear-air turbulence and is expected to aid flight-planning decisions by improving the
28 communication of ensemble-based forecasts to aviation.

29

30 KEY WORDS ash concentration; ash dosage; dispersion modelling; risk matrix; aviation; flight
31 planning; ensemble forecasting

32

33 **1. Introduction**

34 Flight-planning decisions during volcanic eruptions pose many challenges to the aviation
35 industry. An important issue in the decision-making process is the economic impact of grounding
36 and re-routing aircraft during an eruption event and the potential for damage to the engines due
37 to flying in ash clouds at low concentration levels that do not cause an immediate safety risk.
38 While aircraft encounters with volcanic ash are a known safety issue (Casadevall, 1994; Prata
39 and Tupper, 2009; Guffanti and Tupper, 2015), there have been many incidents which suggest
40 that aircraft engines can tolerate low concentrations of ash without catastrophic engine failure. A
41 total of 131 incidents were reported between 1953–2009 and a further 122 were documented for
42 the period from 2010–2016 (Guffanti *et al.*, 2010; Christmann *et al.*, 2017). The increase in
43 documented aircraft encounters between 2010–2016 may be partly a result of better reporting
44 and the publicity of the 2010 Eyjafjallajökull eruption in Iceland. However, as the number of
45 aircraft flying in volcanically active regions around the globe continues to grow—Airbus
46 projects a doubling of passenger aircraft from 2017–2036 (Airbus, 2017)—the number of aircraft
47 encounters with volcanic ash and gas clouds are likely to increase with the potential to lead to
48 serious global economic impacts. In this paper a new way of calculating and communicating
49 volcanic ash forecasts which allows the aviation community to assess the risks associated with
50 flying along a given route and to make flight-planning decisions is presented.

51 The eruptions of Eyjafjallajökull (Iceland) in April and May 2010 had a profound economic
52 impact on the aviation industry. So much so that it prompted changes to the approach taken by
53 regulators towards flying in ash-contaminated airspace. At the time, the International Civil
54 Aviation Organization (ICAO) recommended that all encounters with volcanic ash clouds should
55 be avoided, regardless of the ash concentration (ICAO, 2007). This approach became

56 unworkable during the crisis which put pressure on regulators to re-open controlled airspace
57 where ash concentrations were forecast to be low. In response, the UK Civil Aviation Authority
58 (CAA) in consultation with Rolls-Royce, the UK Met Office, international and European
59 regulators and aviation experts developed quantitative peak concentration limits (Witham *et al.*,
60 2012; Clarkson *et al.*, 2016). Currently, the ICAO EUR/NAT (European and North Atlantic)
61 Volcanic Ash Contingency Plan uses peak concentration limits to define low ($\leq 2 \text{ mg m}^{-3}$),
62 medium ($2\text{--}4 \text{ mg m}^{-3}$) and high ($\geq 4 \text{ mg m}^{-3}$) ash contamination levels (ICAO, 2016). The
63 European Aviation Safety Agency (EASA) and UK CAA have adopted these ash contamination
64 levels and operators are required to have a Safety Risk Assessment approved by their National
65 Aviation Authority before considering entering airspace forecast to contain medium or high ash
66 contamination levels (CAA, 2017).

67 The UK Met Office and Météo-France currently provide quantitative peak concentration
68 forecasts (defined in Section 2) as supplementary information to Volcanic Ash Advisories and
69 Volcanic Ash Graphics issued by the London and Toulouse Volcanic Ash Advisory Centres
70 (VAACs), respectively. Peak concentrations, however, do not take into consideration the
71 situations where an aircraft may be flying through a low concentration ash cloud for a long
72 period of time, which may lead to engine damage (Wylie *et al.*, 2017), or a moderate
73 concentration for a relatively short period of time, which may not lead to engine damage.
74 Volcanic ash dosages represent the accumulated concentration over time along an aircraft's
75 route, thus accounting for the situations above.

76 Recently, Rolls-Royce announced an ash dosage threshold below which exposures will not
77 lead to significant reductions in flight safety margins (Rolls-Royce, 2017). Up to ash
78 concentrations of 4 mg m^{-3} the threshold has been set at a dosage of $14.4 \text{ g m}^{-3} \text{ s}$. This value was

79 calculated based on the assessment that a Rolls-Royce engine should be able to maintain all
80 safety margins after spending 1 h in a concentration of 4 mg m^{-3} or 2 h in a concentration of 2
81 mg m^{-3} . As a result of limitations set by EASA the appropriate dosage above 4 mg m^{-3} has not
82 been defined. These recent developments motivate the need to develop a framework that
83 combines quantitative ash concentration forecasts with air route data to quantify ash dosages
84 along flight paths and their uncertainties.

85 The move to quantitative ash concentration limits has driven rapid development and
86 improvement in volcanic ash concentration forecasting (e.g. Stohl *et al.*, 2011; Dacre *et al.*,
87 2011; Devenish *et al.*, 2012; Millington *et al.*, 2012; Webster *et al.*, 2012). However, dispersion
88 model simulations are subject to various sources of uncertainty which are currently not taken
89 account of by operational deterministic forecasts. Communicating this uncertainty to aviation
90 stakeholders is of prime importance as this information can be used to make better-informed
91 decisions (Mulder *et al.*, 2017).

92 The major sources of uncertainty in volcanic ash transport and dispersion models include
93 uncertainty in the eruption source parameters (e.g. mass eruption rate and plume height), internal
94 model parameterisations (e.g. wet deposition and free tropospheric turbulent mixing) and the
95 driving meteorology (Folch, 2012; Harvey *et al.*, 2018). The challenge is then to develop a
96 robust methodology which accounts for these uncertainties objectively, but also allows for fast
97 decisions to be made by operators and regulators. Robust decisions from quantitative data require
98 a measure of their uncertainties. A common method for representing uncertainty in weather
99 forecasting is to develop an ensemble: a set of model realisations created by perturbing various
100 uncertain parameters used at the start of each model run (e.g. Palmer, 2002; Buizza *et al.*, 2005;
101 Gneiting and Raftery, 2005). An ensemble (probabilistic) forecast allows for a robust decision as

102 it can be used to quantify the likelihood of a certain event occurring. It is therefore logical to
103 extend ensemble forecasting methods to dispersion modelling of volcanic ash concentrations. An
104 example in the context of the ash–aviation problem would be the likelihood of the ash
105 concentration being above a certain threshold. However, too much (or too complex) information
106 can prevent a decision-maker from making a fast decision, which is generally a requirement in
107 operational settings. This issue is often referred to as ‘information overload’ and was raised as a
108 major concern by operators and regulators during and following the 2010 Eyjafjallajökull crisis.

109 The UK Met Office National Severe Weather Warning Service utilises the concept of a risk
110 matrix to communicate ensemble-based forecasts of severe weather events to the public (Neal *et*
111 *al.*, 2014). *Risk* is defined as the product of the *likelihood* and *impact* of an event occurring. A
112 risk matrix is constructed by discretising likelihoods and impacts into different ranges and
113 assigning a risk severity to each combination of the impact and likelihood ranges. This approach
114 addresses the issue of information overload by condensing probabilistic information into
115 appropriate courses of action to be taken by the relevant stakeholders (e.g. the public, an airline
116 operator, emergency services etc.). In the present study, this approach is adapted to the ash–
117 aviation problem by considering ash dosage and peak concentration as *impact* and using
118 ensemble modelling to quantify their *likelihood*.

119 The aim of this paper is to develop a proof-of-concept methodology for implementing a risk-
120 based approach to flight planning; using ash dosage and concentration encountered by an aircraft
121 along its flight path (hereafter known as ‘along-route ash dosage and/or concentration’). To
122 generate ash concentration data, a hypothetical Icelandic eruption scenario resulting in ash
123 dispersal across the North Atlantic was simulated using the dispersion model used operationally
124 by the London VAAC (LVAAC). Trans-Atlantic air routes were generated using time-optimal

125 routing software to simulate ash encounters permitting ash dosage calculations. An ensemble
126 dataset was developed (based on uncertainty in the meteorology, eruption source parameters and
127 internal model parameterisations) to estimate the likelihood of certain ash dosage and peak
128 concentration ranges. The ash dosage risk was then calculated for various flight routes to
129 demonstrate how airline operators might use this information.

130 **2. NAME model setup**

131 The Numerical Atmospheric-dispersion Modelling Environment (NAME; Jones *et al.*, 2007) is a
132 Lagrangian dispersion model used operationally by the LVAAC. The Lagrangian representation
133 of atmospheric dispersion within NAME allows for each model particle to be tracked as it is
134 advected by the three-dimensional wind fields. If the size (volume), shape and density of a
135 particle are known its mass can be calculated. Mass concentration fields are calculated in NAME
136 by dividing the total mass of particles in a given grid box by its volume.

137 In the present study, NAME (version 6.5) was used to simulate a hypothetical Icelandic
138 eruption using the default setup of the LVAAC. Ash (mass) concentrations were output onto a
139 global grid of 800 by 600, corresponding to a grid resolution of approximately 0.451° longitude
140 by 0.301° latitude (~ 40 km horizontal resolution), at 22 flight levels (FL) from FL000 to FL550
141 (1013.25 to 91.15 hPa) with a vertical resolution of 25FL. Note that flight levels are defined as
142 standardised pressure altitudes expressed in units of hundreds of feet and are based on the ICAO
143 standard atmosphere. The concentration fields were output every 6 h using a 6 h time average
144 with a total run time of 66 h. The eruption plume was defined as a uniformly distributed vertical
145 line source extending from the volcano summit to the eruption plume height and the particle
146 release rate was set to 15000 h^{-1} , which is consistent with the model set up at the LVAAC
147 (Witham *et al.*, 2016). Finally, to convert to peak concentrations, the mean ash concentration

148 fields output by NAME were multiplied by a factor of 10. This is known as the ‘peak-to-mean’
149 factor and has been adopted by the LVAAC to account for peak concentrations that cannot be
150 resolved by the NAME model (Webster *et al.*, 2012). This model configuration is referred to as
151 the ‘thin layer’ setup hereafter and is equivalent to the ‘25FL layer scheme’ described in Webster
152 *et al.* (2012). The output from the thin layer setup in NAME was then post-processed to produce
153 the LVAAC’s ‘thick layer’ product. The ‘thick layer’ product was produced by dividing the
154 vertical grid into three flight level ranges (FL000–FL200, FL200–FL350 and FL350–FL550) and
155 then setting the maximum ash concentration of the thin layers (25FL thickness) within each
156 range to the concentration of each thick layer (Figure 1).

157 2.1. Meteorological data

158 The meteorological data that were used to drive NAME includes two datasets: an analysis dataset
159 produced by the Met Office Unified Model (MetUM; Cullen, 1993; Brown *et al.*, 2012) and an
160 ensemble dataset produced using the European Centre for Medium-Range Weather Forecasts
161 (ECMWF) Integrated Forecast System (IFS) (Buizza *et al.*, 1999). The MetUM analysis fields
162 have a horizontal resolution of ~ 17 km and vertical resolution of ~ 0.7 km in the upper
163 troposphere/lower stratosphere (UTLS). The time resolution of the MetUM data is 3 hourly
164 alternating from analysis to forecast fields every 3 h. At time intervals smaller than 3 h, the
165 meteorology fields are linearly interpolated. The MetUM dataset was used to drive NAME for
166 the control run (described in Section 2.2). The ECMWF IFS (cycle 43r1) was used to create an
167 ensemble of forecast meteorology. These data were archived at a horizontal resolution of 16 km
168 (T1279 spectral truncation) and vertical resolution of ~ 1.4 km in the UTLS with a time
169 resolution of 3 h and forecast lead-time of 66 h. These data were then extracted onto a regular
170 latitude/longitude grid of 0.125° by 0.125° and the precipitation, surface stresses and sensible

171 heat flux fields were post-processed so that they could be read in by NAME. To account for
172 uncertainty in the initial meteorological fields, the ECMWF IFS Ensemble Prediction System
173 (EPS) was used to produce a 20-member meteorological ensemble. The EPS utilises the singular-
174 vector approach (Buizza and Palmer, 1995) to perturb initial conditions in the meteorology and a
175 stochastic physics scheme (Buizza *et al.*, 1999) to account for model uncertainty. The ECMWF
176 dataset was used to investigate four sources of uncertainty in dispersion modelling: eruption
177 source parameters, internal NAME model parameters, initial meteorological conditions and error
178 growth with increasing forecast lead-time.

179 2.2. Icelandic eruption scenario

180 The parameters used to define an eruption in NAME are referred to as eruption source
181 parameters (ESPs). These include the timing, location, duration, plume height, geometry and
182 vertical ash distribution of each eruptive phase during an event as well as the mass eruption rate
183 (MER) and microphysical properties of the distal fine ash particles (shape, density and size
184 distribution). In the following, the control run ESPs for the Icelandic eruption scenario are
185 described.

186 An explosive eruption from an Icelandic volcano has the potential to release volcanic ash at
187 aircraft cruising altitudes. Depending on the weather conditions, this type of eruption could result
188 in widespread ash dispersal across the North Atlantic and neighbouring landmasses, disrupting
189 trans-Atlantic air-traffic. The Katla volcano (19.083 ° W, 63.633 ° N, 1490 m a.s.l.) was selected
190 for the eruption scenario as it is an active volcano in Iceland with the potential for an explosive
191 ash-rich eruption. The eruption plume height was set to 15 km a.s.l. with a duration of 16 h to
192 ensure significant ash dispersal at cruise altitude (~10 km). Following the current approach of the
193 LVAAC, the MER was calculated from the plume height using the empirically-derived Mastin *et*

194 *al.* (2009) relationship. As the total grain size distribution is not modelled in NAME, the fraction
195 of mass due to fine ash (diameters $\leq 100 \mu\text{m}$) must be considered. This is known as the distal
196 fine ash fraction (DFAF) and is also included as an ESP here. As the DFAF is the percentage of
197 mass assumed to remain in the atmosphere after an initial eruption, the MER is scaled by this
198 percentage. A DFAF of 5% was chosen as this is the default value used by the LVAAC for an
199 Icelandic eruption (Witham *et al.*, 2016). Similarly, the LVAAC's default ash size distribution
200 was used (see Witham *et al.*, 2016 Table 1) and the shape of the particles were assumed to be
201 spherical.

202 The eruption start time was set to 1 January 2017 at 0300 UTC as during this time an upper-
203 level ridge had formed over Iceland and the North Atlantic Ocean. This winter-time weather
204 regime is representative of the W3 and W4 categories identified by Irvine *et al.* (2013) as
205 frequent modes of variability in the North Atlantic. This meteorological situation occurs one
206 third of the time during the winter months and is characterised by northerly flow from Iceland
207 and persistent anticyclonic flow over the North Atlantic. In this scenario, volcanic ash from an
208 Icelandic eruption is dispersed toward the south and circulated over the North Atlantic for
209 several days. Due to large scale subsidence there is very little precipitation in this scenario and so
210 the amount of wet deposition is expected to be small. The control run ESPs are summarised in
211 Table 1 and the evolution of the ash cloud over 66 h in the control run simulation for the thick
212 layer concentrations from FL350–FL550 is shown in Figure 2.

213 **3. Ensemble simulations**

214 There are many ways to represent uncertainty in model simulations. In this paper, an ensemble of
215 NAME simulations is created by varying the meteorology, ESPs and internal model parameters.
216 Latin Hypercube Sampling (LHS; Iman and Conover, 1980) is a statistical technique that can be

217 used to efficiently generate an ensemble which ensures orthogonality between input model
218 parameter sets. The LHS method was used to generate a Latin Hypercube with 9 dimensions (i.e.
219 9 dispersion model input parameters were varied) and was sampled 600 times resulting in an
220 ensemble of 600 members. These simulations were conducted on the JASMIN ‘super-data-
221 cluster’ (Lawrence *et al.*, 2012) and took less than 1 h to complete for a 24-h ensemble forecast.
222 This runtime (and ensemble size) potentially allows an operational VAAC to provide 24 h
223 ensemble forecasts every 6 h; provided that they have sufficient computer resources and an
224 operational meteorological ensemble prediction system set up. All model parameters considered
225 in the LHS analysis were sampled from a uniform distribution. By sampling from a uniform
226 distribution, it is assumed that all values between their specified ranges are equally likely. The 9
227 model parameter choices (and their specified ranges) are listed in Table 1 and are described in
228 the following sections.

229 3.1. Meteorological initial conditions and forecast error growth

230 It has been demonstrated that even for short lead-time forecasts (< 72 h) small differences in the
231 forecast wind fields can lead to large spread in the forecast ash clouds (Dacre and Harvey, 2018).
232 As described in Section 2.1, uncertainty in the initial meteorological fields as well as error
233 growth in the forecast fields were represented using the ECWMF dataset. These data make up a
234 20-member ensemble of meteorology. For the LHS sampling, ECMWF members were sampled
235 from a uniform distribution between 0 and 19. The random variable sampled from this range was
236 then rounded to the nearest integer. This index was then used to select (at random) an ECMWF
237 ensemble member for each of the 600 parameter sets.

238 3.2. Eruption source parameters

239 To represent the uncertainty associated with the ESPs, a range of uncertainty (i.e. maximum and
240 minimum values) was assigned to each control run ESP and then randomly sampled from a
241 uniform distribution between the specified ranges (Table 1). The plume height, DFAF and MER
242 were selected for the LHS analysis as output from NAME has been shown to be the most
243 sensitive to these parameters (e.g. Dacre *et al.*, 2011; 2013; Harvey *et al.*, 2018). The source
244 timing (i.e. eruption onset) and duration were chosen to illustrate how uncertainty in these
245 parameters can lead to uncertainty in the timing and location of the modelled ash cloud.

246 The ranges selected for each ESP were made based on typical ranges reported in the
247 literature (e.g. Mastin *et al.*, 2009; Devenish *et al.*, 2012; Dacre *et al.*, 2013; Harvey *et al.*, 2018).
248 It is acknowledged that there is a degree of subjectivity in these choices; however, their specific
249 values do not alter the methodology developed to implement a risk-based approach (described in
250 Section 6) that can be used for making robust and fast flight-planning decisions.

251 3.3. Internal model parameters

252 Dacre *et al.* (2015) have shown that the internal model parameters used in NAME to represent
253 free tropospheric turbulence can significantly impact the vertical depth (thickness) of volcanic
254 ash clouds and hence peak concentrations. These internal model parameters were also
255 investigated by Harvey *et al.* (2018) and were demonstrated to be the largest internal model
256 parameter contribution to uncertainty in NAME output. To represent uncertainty in free
257 tropospheric turbulence, the standard deviation (σ) and Lagrangian timescales (τ) of the
258 horizontal and vertical velocity components were sampled from a uniform distribution using the
259 range specified in Harvey *et al.* (2018). The horizontal and vertical components of these
260 parameters were varied in proportion to each other so that the shape of the turbulent eddies
261 parameterised in NAME is preserved. It is also noted that the horizontal component of standard

262 deviation of the free tropospheric turbulence was sampled on a logarithmic scale. Finally, the
263 standard deviation of the horizontal velocity for unresolved mesoscale motions was also sampled
264 from a uniform distribution following the ranges used in Harvey *et al.* (2018).

265 **4. Along-flight ash dosage**

266 To simulate aircraft encounters with volcanic ash, flight routes were generated using time-
267 optimal routing software developed by Irvine *et al.* (2016), which was based on the methodology
268 of Lunnon and Marklow (1992). The ‘flightCode’ program uses latitude and longitude pairs
269 representing the origin and destination airports for a given route, the constant true airspeed of the
270 aircraft and horizontal wind data at a given flight level. The code assumes that the aircraft is at a
271 fixed altitude and so take-off and landing are not considered. The output of flightCode is a set of
272 waypoints (latitude and longitude pairs) representing the fastest (time-optimal) route for the
273 specified airport pairs at a given instance in time given the prevailing wind at a given altitude.

274 In the present analysis, trans-Atlantic flights were generated assuming a constant true
275 airspeed of 250 m s^{-1} (900 km h^{-1}) and the MetUM dataset was used to provide horizontal wind
276 data at FL350 (assumed to be the cruise altitude of the aircraft). The eastbound and westbound
277 time-optimal routes from New York (JFK) to London (LHR) were calculated for each time step
278 of the dispersion model output (i.e. at 6 h intervals for 11 time steps).

279 The along-flight ash dosage is defined as the ash concentration multiplied by the time spent
280 in that concentration (duration of exposure) along an aircraft’s flight path, which means that the
281 dosage, D , is expressed in units of grams per cubic metre seconds ($\text{g m}^{-3} \text{ s}$):

$$D = \sum_{i=1}^n C_i \Delta t_i = \sum_{i=1}^n C_i \frac{\Delta s_i}{V_a} \quad (1)$$

282 where n is the number of dispersion model grid boxes intersected by the air route, Δt_i is the
 283 duration of exposure in the i th grid box, C_i is the ash concentration of the i th grid box
 284 intersected, Δs_i is the distance travelled through the i th grid box and V_a is the true airspeed of the
 285 aircraft. This definition means that dosage always increases monotonically along the route and is
 286 distinct from Peterson and Dean (2007) who use ‘ash exposure’ (g m^{-2}) to quantify the potential
 287 damage to aircraft intersecting ash clouds and Prata and Prata (2012) who defined dosage as the
 288 accumulated mass of ash (g) along an aircraft’s route. The definition adopted here ($\text{g m}^{-3} \text{ s}$) is
 289 consistent with the definitions used in Kristiansen *et al.* (2015), Clarkson *et al.* (2016), Wylie *et*
 290 *al.* (2017) and Prata *et al.* (2018); however, Clarkson *et al.* (2016) refer to dosage as a ‘dose’ in
 291 their paper. All dosage calculations reported here assume that the modelled ash concentration
 292 fields at a given time step are static (i.e. do not change with time) as the aircraft flies from the
 293 origin to destination at its true airspeed. Note also that these ash concentrations correspond to the
 294 post-processed ash concentrations at the FL350–FL550 thick layer level (described in Section 2)
 295 and may result in overestimates of the along-route dosage at FL350 due to the application of the
 296 peak-to-mean ratio and the approach of taking the maximum concentration of the thin layers
 297 between FL350 and FL550 when determining the ‘thick layer’ concentration.

298 **5. Representation of uncertainty**

299 5.1. Model agreement maps

300 The ensemble simulations (described in Section 3) were used to calculate the likelihoods of ash
 301 concentrations exceeding different thresholds, based on output from NAME. Specifically, the

302 likelihoods represent the percentage of ensemble members that predicted an ash concentration
303 above a certain peak concentration threshold. Based on discussions with regulators and operators
304 these likelihoods were split into three ranges: less likely (0–10%), likely (10–90%) and very
305 likely (90–100%). It is noted that while regulators and operators suggested a three-category
306 system, the actual values of these boundaries were chosen by the authors to illustrate the present
307 method. In an operational setting, these values may be altered by the user to reflect their risk
308 appetite. Given that these percentages represent the level of agreement between ensemble
309 members these maps are referred to hereafter as ‘model agreement maps’ and do not strictly
310 constitute likelihoods. For ensemble simulations to represent true likelihoods they should be
311 calibrated using past observations and forecasts. However, in order to illustrate the proof-of-
312 concept risk matrix method in this paper, uncalibrated ‘model agreement’ values are used to
313 represent ‘likelihoods’ (described in Section 6). The likelihood boundaries represented on the
314 model agreement maps, however, depend on the ash concentration threshold chosen. The choice
315 of threshold was raised in meetings with various aviation stakeholders and thresholds ranging
316 from 0.2–10 mg m⁻³ were suggested.

317 To demonstrate how model agreement maps depend on ash concentration thresholds, four
318 model agreement maps (for FL350–FL550 at T+30) were generated; corresponding to four ash
319 concentration thresholds: 0.2, 2, 4 and 10 mg m⁻³. Figures 3(a)–(d) show both the horizontal and
320 vertical model agreement maps for each of the peak concentration thresholds analysed. Note that
321 the vertical cross-sections were constructed by first calculating the time-optimal route at FL350
322 from JFK to LHR (return) and then calculating the ash concentration along this route for each
323 thick layer level. The ash concentration contours corresponding to each peak concentration

324 threshold from the control run are also overlaid on Figures 3(a)–(d) to demonstrate where an ash
325 cloud boundary might be drawn for a single (deterministic) forecast.

326 The horizontal model agreement maps reveal regions where there is high confidence in the
327 location of the ash cloud and concentration and regions where there is low model confidence.
328 Figure 3(a) shows the 0.2 mg m^{-3} ash concentration contour for the control run, which may be
329 used to determine the extent of a modelled ash cloud (Witham *et al.*, 2012). The model
330 agreement map indicates that over the western part of the British Isles a considerable percentage
331 ($>10\%$) of ensemble member simulations contained ash above 0.2 mg m^{-3} whereas the control
332 simulation (black line) did not. This result demonstrates that, for this scenario, a single
333 (deterministic) model simulation would not have forecast ash concentrations above 0.2 mg m^{-3}
334 over this region while the ensemble, which accounts for uncertainty in the deterministic
335 simulation, shows that ash over this region was ‘likely’ (10–90%). Comparison of the different
336 ash concentration thresholds demonstrates that when the threshold is increased the region of
337 uncertainty increases relative to the control run (deterministic forecast). This is illustrated by
338 Figure 3(d) where the control run contour of 10 mg m^{-3} covers a small region over the middle
339 section of the westbound flight path and the ensemble indicates that ash concentrations above 10
340 mg m^{-3} are ‘likely’ (10–90%) over a larger region of the North Atlantic. The region of
341 uncertainty relative to the control run also increases with increasing ash concentration threshold
342 for the vertical model agreement maps, where this approach quantitatively shows the degree of
343 confidence in the model for ash concentrations at the three thick layer regions. In the bottom
344 panel of Figure 3(a), at approximately 5000 km along the route, the control run simulation
345 indicates ash at low altitudes; however, the model agreement contours indicate that $> 10\%$ of the

346 ensemble members resulted in ash concentrations above 0.2 mg m^{-3} at cruise altitude (FL350–
347 FL550 thick layer level).

348 In general, the area covered by each likelihood category was reduced as the ash concentration
349 threshold was increased (compare Figures 3(a)–(d)); however, the uncertain region over the
350 western part of the British Isles remained largely the same for thresholds up to 10 mg m^{-3}
351 (Figures 3(a)–(d)). This indicates that 10–90% of the ensemble members forecast ash
352 concentrations above 10 mg m^{-3} over this region (Figure 3(d)).

353 5.2. Model agreement along routes

354 The ensemble approach can also be used to represent the uncertainty in ash dosage calculations.
355 However, as the dosage is calculated along a flight path, the model agreement values are
356 displayed as the percentage of ensemble members that predict the dosage to be above a certain
357 dosage threshold along the air route. Figure 4(a) shows the model agreement along the route
358 from JFK–LHR (return) at FL350–FL550 and T+30 using the Rolls-Royce airworthiness
359 threshold of $14.4 \text{ g m}^{-3} \text{ s}$. When the model agreement is calculated along the route, the likelihood
360 of the aircraft engine exceeding the dosage threshold increases along the route. For comparison,
361 Figure 4(b) shows the same model agreement along the route but for a doubling of the dosage
362 threshold (i.e. $28.8 \text{ g m}^{-3} \text{ s}$). As with the ash concentration model agreement maps, when the
363 dosage threshold is increased, the likelihood categories are affected. For this example, when the
364 dosage threshold is doubled, the distance the aircraft can travel while remaining in the ‘likely’
365 category increased by a small amount while the distance travelled in the ‘very likely’ category
366 reduced (compare Figures 4(a) and (b) at the location of the westbound aircraft). This small
367 difference suggests that an operator may make a similar decision for both dosage thresholds for

368 this particular scenario. However, for a different air-route or eruption scenario a change in the
369 dosage threshold may have more of an effect on the likelihood boundaries.

370 Displaying model agreement as maps and along air routes provides aviation stakeholders
371 with a new method for displaying ensemble-based ash concentration and dosage information.
372 While this approach has been demonstrated for the JFK–LHR route, operators could apply the
373 same analysis to different or multiple flight tracks. The main advantage in displaying the data
374 this way is that decision-makers are provided with information about the confidence of the model
375 forecasts, which may improve flight-planning procedures.

376 **6. Risk maps and routes**

377 While the concept of model agreement is useful in that it can be used to indicate the likelihood of
378 a given impact (e.g. ash concentration and dosage) at a certain flight level and time, multiple
379 figures must be generated for varying thresholds of interest and may prevent an operator from
380 making a fast decision due to information overload. A risk-based approach has been shown to
381 reduce this issue for other hazards by condensing the ensemble information into a single map
382 (e.g. Neal *et al.*, 2014); thereby permitting multi-layered information in operational settings and
383 providing the users with the relevant information needed to make a decision.

384 **6.1. Ash concentration risk matrix**

385 To construct a risk matrix both the impact and likelihood of the hazard must be combined
386 (shown schematically in Figure 5(a)). For the ash concentration risk matrix, the impact was
387 defined based on the following ash concentration (C) ranges (in mg m^{-3}): $0.2 < C \leq 2$, $2 < C <$
388 4 and $C \geq 4$. For the likelihood ranges, the same ranges in Section 5 were used: 0–10 % (less
389 likely), 10–90 % (likely) and 90–100 % (very likely); resulting in a 3 by 3 matrix (Figure 5(b)).

390 The boxes in the risk matrix each correspond to a different combination of impact and
 391 likelihood. Following the approach of Neal *et al.* (2014), each box was assigned a colour using a
 392 three-colour warning system (yellow, amber and red). The colours then correspond to a decision
 393 to be made or action to be taken by the stakeholder. For example, if it is very likely (90–100%)
 394 that the peak concentration will be low ($0.2\text{--}2\text{ mg m}^{-3}$) the risk level is shown in the top left box
 395 of the ash concentration risk matrix (Figure 5(b)). The decision of a flight-planner in this
 396 situation might be to allow the aircraft to fly its scheduled route and continue to check updated
 397 forecasts. On the other hand, if it is very likely (90–100%) that the peak concentration will be
 398 high ($\geq 4\text{ mg m}^{-3}$) the risk level is shown in the top right box of the matrix. In this situation a
 399 different action might be taken such as re-routing the aircraft. To illustrate how the risk matrix
 400 might be used to make fast and robust decisions, the following example actions were assigned to
 401 each colour warning (Figure 5(c)):

- 402 1) Yellow = Schedule route; check updated forecasts
- 403 2) Amber = Load more fuel; check updated forecasts; perform engine checks
- 404 3) Red = Consider alternative routes

405 Figures 6(a) and (b) show risk maps in the horizontal and vertical, respectively, for the same
 406 valid meteorological time and altitude shown in Figure 3. Note that at each location on the risk
 407 maps the colour warning corresponding to the maximum risk level is shown. For example, in a
 408 location where the likelihood of the ash concentration exceeding 4 mg m^{-3} is less likely (i.e. an
 409 amber warning) and the likelihood of the ash concentration being $0.2\text{--}2\text{ mg m}^{-3}$ is likely (yellow
 410 warning), the latter is ignored in favour of the higher risk level. The horizontal risk map (Figure
 411 6(a)) shows that amber and red warnings would be issued for airspace over the western part of
 412 the British Isles while the areas between Iceland and the British Isles and over large parts of the

413 North Atlantic would be issued with red (high risk) warnings. In this situation, the decision for
414 aircraft planning routes over the amber regions of the risk map could be to load more fuel and
415 perform engine checks. Figure 6(b) shows that aircraft flying the time-optimal eastbound and
416 westbound routes between JFK and LHR at cruise altitude (FL350–FL550) would fly through
417 high risk regions; this means that alternative routes should be considered.

418 The risk-based approach to ash concentrations demonstrates how the four maps of Figure 3
419 can be condensed into one single figure, which can be used to make fast decisions and overcome
420 the issue of information overload for operators. It can also be used to see why each warning is
421 issued by illustrating which box in the risk matrix a particular location of interest corresponds to.
422 For example, the location annotated with a ‘+’ within the amber region southwest of the British
423 Isles in Figures 7(a) and (b) corresponds to the bottom right box in the ash concentration risk
424 matrix. This means that $\leq 10\%$ of the ensemble member simulations resulted in ash
425 concentrations greater than or equal to 4 mg m^{-3} at this location. The risk-based approach allows
426 for multiple layers of information about the ensemble of ash concentration forecasts. This is
427 useful, for example, in an operational environment where a simple colour warning may be
428 required for operators and regulators to take fast or immediate action. Intermediate information is
429 displayed by identifying a location in the risk matrix. This allows decision makers to distinguish
430 between, for example, amber warnings generated from a less likely ($\leq 10\%$), high impact (≥ 4
431 mg m^{-3}) forecast and a likely (10–90%), medium impact (2–4 mg m^{-3}) forecast.

432 6.2. Ash dosage risk matrix

433 The ash concentration risk, however, does not consider the potential risk of flying through low
434 ash concentrations for long durations of exposure or the potential to fly through high ash
435 concentrations for short durations of exposure without experiencing engine damage. To account

436 for these situations a dosage risk matrix was constructed (Figure 5(d)). The ash dosage, D ,
437 impact was defined by the following ash dosage boundaries (in $\text{g m}^{-3} \text{ s}$): $1.44 < D \leq 14.4$,
438 $14.4 < D < 28.8$ and $D \geq 28.8$ and the likelihood ranges were the same as those used for the
439 ash concentration risk matrix.

440 Figure 7(a) shows the along-route dosage risk corresponding to the dosage risk matrix
441 described above. Visualising the dosage risk along the route shows that an aircraft flying from
442 JFK to LHR return is predicted to encounter a region of high risk towards the end of the
443 eastbound section of the flight. In this case, a flight-planner may decide to ‘consider alternative
444 routes’ for the aircraft based on the red colour warning (Figure 5(c)).

445 This method can also be adapted so that both along-route dosage and peak concentration risk
446 are taken into account (Figure 7(b)). In this approach, the risk level corresponding to the higher
447 risk is selected. For example, in the section of the eastbound route between 40° W and 30° W
448 the peak concentration-based risk is higher than the dosage-based risk and so the route is
449 coloured according to the ash concentration-based risk level. This approach assumes that a high
450 peak concentration should be considered a high risk to the aircraft regardless of the duration of
451 exposure and is therefore more restrictive than using the dosage alone to determine the risk.
452 Current advice from Rolls-Royce is to perform engine checks if an aircraft is suspected to have
453 flown through peak concentrations greater than or equal to 4 mg m^{-3} and that dosages are a more
454 appropriate measure of engine susceptibility to volcanic ash (Clarkson and Simpson, 2017).

455 Figure 7(c) shows the full range (minimum and maximum) of possible along-route ash
456 concentrations and dosages generated from the ensemble for an aircraft flying through the thick
457 layer level (FL350–FL550) at T+30. The range of dosages produced by the ensemble was from
458 $4.5\text{--}2000 \text{ g m}^{-3} \text{ s}$ (median of $160 \text{ g m}^{-3} \text{ s}$) and the range of peak ash concentrations was from 0–

459 670 mg m⁻³ (ensemble median maximum of 38 mg m⁻³). Analysis of the probability density
460 functions (PDFs) of the maxima of the along-route ash concentration and dosage shows that
461 these variables follow lognormal distributions (Figures 8(a), (b)). The along-route ash
462 concentration and dosage ensemble maxima (upper bounds of the shaded regions in Figure 7(c))
463 are therefore representative of rarely occurring extreme values. The occurrence of extreme
464 values in the ensemble, however, does not preclude the use of a risk matrix. To understand how
465 the risk warning is determined from the distribution of the ensemble, these data can be
466 represented by ‘risk PDFs’ (Figures 8(c), (d)) using ash concentration and dosage risk matrices.
467 Here the elements of the risk matrix are assigned numerical values (1–9) and the highest risk
468 value intersected by the distribution (re-binned according to the risk matrix impact boundaries)
469 determines the risk level. This approach has recently been suggested for a probabilistic, multi-
470 level wildfire warning system in Chile (Dacre *et al.*, 2018). An alternative, less conservative,
471 approach could be to use the mean or modal risk level. Figures 8(c) and (d) show that while
472 extreme values are present in the ensemble, the majority (> 90%) of the along-route ash
473 concentration and dosage maxima also exceed the maximum impact boundaries of the risk
474 matrices (defined in Sections 6.1 and 6.2). Therefore, one could be confident in a red risk
475 warning issued for the maximum ash concentration and dosage encountered along a return route
476 from JFK-LHR at FL350–FL550 and T+30. The advantage of this third layer of information is
477 that the forecaster can identify when the risk warning is due to outliers (i.e. a small number of
478 ensemble members predicting a high impact) and when the risk warning is confident (i.e. all
479 members predicting the same impact). Thus, even though the LHS dispersion model ensemble
480 members spanned several orders of magnitude in both the along-flight ash concentration and

481 dosage, the risk-based approach can still be used by flight-planners to make fast and robust
482 decisions.

483 **7. Discussion and conclusions**

484 The methodology described in this paper has been developed to show how a dispersion
485 model ensemble can be used to make fast and robust decisions during a hypothetical Icelandic
486 eruption scenario. The ability to make fast decisions, however, is contingent upon the forecast
487 service organisation having the computer resources necessary to conduct an ensemble forecast in
488 a short period of time. The method was applied to both volcanic ash concentrations and dosages.
489 To permit dosage calculations, aircraft routing software was used to generate time-optimal
490 eastbound and westbound trans-Atlantic flights from New York to London through a simulated
491 ash cloud over the North Atlantic.

492 To characterise the likelihood of certain ash concentration and dosage thresholds, the
493 concept of model agreement was used. Model agreement values rely on setting ash concentration
494 and dosage thresholds and were shown to be useful in visualising model confidence. Comparison
495 of the control run and the model agreement maps highlighted the importance of quantifying the
496 uncertainty in a deterministic forecast with an ensemble. In an operational context, these maps
497 could be used to plan flight paths closer to the ash cloud boundary in regions where model
498 confidence (agreement) is high than in regions where model confidence is low. This method is an
499 improvement to the subjective approach where the decision-maker infers their own uncertainty
500 by drawing a buffer (typically of uniform distance) around the deterministic ash cloud boundary
501 to indicate their perceived confidence in an ash concentration forecast (e.g. Mulder *et al.*, 2017).

502 To address the issue of information overload, risk matrices for both ash concentration and
503 dosage were constructed. These were used to demonstrate how fast decisions can be made when
504 taking uncertainty information into consideration. The risk matrix relies upon two key choices:
505 the choice of the likelihood boundaries and the choice of the impact (dosage and/or ash
506 concentration) boundaries. The choice of the likelihood and impact boundaries shown here were
507 based on discussions with aviation stakeholders and illustrate how this method can be
508 implemented. In an operational setting, these boundaries would be set prior to an eruption by the
509 user to reflect their risk appetite. One of the key advantages of this approach is that it allows the
510 user to make decisions even when faced with large sources of uncertainty in the model forecasts.
511 Additionally, visualising the dosage risk along the aircraft's route may be useful on an airline
512 operator fleet-scale where multiple risk routes are viewed on the same map.

513 The risk-based approach also encompasses varying levels of complexity. As shown with
514 the amber region example, an aircraft pilot may just require a colour warning to respond to the
515 hazard, while a dispersion modelling expert can query further to see what combination of
516 likelihood and impact caused the colour warning. A third step can be taken by looking at risk
517 probability density functions to identify when the risk warning is a result of outliers in the
518 ensemble and when the risk warning is confident. To effectively communicate this approach to
519 aviation stakeholders, the Volcanic Dosage And Risk Tool (VDART) has been developed
520 (accessible at <http://www.met.reading.ac.uk/ash-dosage>). The VDART interface has been
521 designed as a demonstration tool to illustrate how probabilistic forecasts of ash concentration and
522 dosage risk can be used to make fast and robust decisions. The web-tool was developed in
523 collaboration and consultation with aviation industry regulators, operators, engine manufacturers

524 and the UK Met Office and takes advantage of interactive data visualisation to communicate
525 uncertainty information.

526 Finally, this approach could potentially be applied to historical eruptions or extended to
527 other aviation hazards such as SO₂ and desert dust dosages or meteorological hazards such as
528 aircraft icing and clear-air turbulence. In cases where the model parameters are well constrained,
529 the ensemble could also be used for post-analysis when an engine manufacturer or airline
530 operator is trying to diagnose the likely range of dosages their engines have been exposed to.

531 **Acknowledgements**

532 This research is funded by Natural Environment Research Council (NERC) under the
533 Environmental Risks to Infrastructure Innovation Programme (NE/P009026/1). Colin Hord,
534 Andy Wells and David Gibbs of the UK Civil Aviation Authority are thanked for explaining the
535 current guidance for flight operations in the vicinity of volcanic ash and for facilitating
536 discussions with the aviation industry. Capt John Monks of British Airways is acknowledged for
537 providing an operators' perspective on flight operations during volcanic ash events. Dr Natalie
538 Harvey (University of Reading) is thanked for providing her expertise on running the NAME
539 model and advice on how to perturb the eruption source and internal model parameters
540 considered in this paper. Dr Helen Thomas (University of Bristol) is thanked for valuable
541 discussions on volcanic ash dosages and comments on the web-tool. The UK Met Office is
542 acknowledged for use of the NAME dispersion model and Drs Matthew Hort, Claire Witham
543 and Frances Beckett (UK Met Office) are thanked for discussions of the results and guidance on
544 the operational LVAAC setup of NAME. Members of the World Meteorological Organization
545 (WMO)/International Union of Geodesy and Geophysics (IUGG) Volcanic Ash Science

546 Advisory Group (VASAG) are also acknowledged for their constructive comments on the web-
547 tool. Finally, two anonymous reviewers are thanked for their comments which led to significant
548 improvements to the manuscript. NAME simulation output presented in this paper is available on
549 the University of Reading Research Data Archive (accessible at
550 <http://dx.doi.org/10.17864/1947.148>).

551

552 **References**

- 553 Airbus 2017. *Airbus Global Market Forecast 2017–2036 “Growing horizons.”* Airbus SAS:
554 Blagnac, France. [http://www.airbus.com/content/dam/corporate-
555 topics/publications/backgrounders/Airbus_Global_Market_Forecast_2017-
556 2036_Growing_Horizons_full_book.pdf](http://www.airbus.com/content/dam/corporate-
555 topics/publications/backgrounders/Airbus_Global_Market_Forecast_2017-
556 2036_Growing_Horizons_full_book.pdf) (accessed 17 November 2017).
- 557 Brown A, Milton S, Cullen M, Golding B, Mitchell J, Shelly A 2012. Unified modeling and
558 prediction of weather and climate: A 25-year journey. *B. Am. Meteorol. Soc.* **93**:1865–1877.
- 559 Buizza R, Palmer TN 1995. The Singular-Vector Structure of the Atmospheric Global
560 Circulation. *J. Atmos. Sci.* **52**:1434–1456.
- 561 Buizza R, Houtekamer PL, Toth Z, Pellerin G, Wei MZ, Zhu YJ 2005. A comparison of the
562 ECMWF, MSC, and NCEP global ensemble prediction systems. *Mon. Weather Rev.*
563 **133**:1076–1097.
- 564 Buizza R, Miller M, Palmer TN 1999. Stochastic representation of model uncertainties in the
565 ECMWF Ensemble Prediction System. *Q. J. R. Meteorol. Soc.* **125**:2887–2908.
- 566 CAA 2017. *CAP1236: Guidance regarding flight operations in the vicinity of volcanic ash.* Civil
567 Aviation Authority: Aviation House, Gatwick Airport South, UK.

568 <http://publicapps.caa.co.uk/docs/33/CAP%201236%20FEB17.pdf> (accessed 17 November
569 2017).

570 Casadevall TJ 1994. *Volcanic Ash and Aviation Safety: Proceedings of the First International*
571 *Symposium on Volcanic Ash and Aviation Safety*. U.S. Geol. Surv. Bull. 2047.

572 Christmann C, Nunes RR, Schmitt AR, Guffanti M 2017. Flying into Volcanic Ash Clouds: An
573 Evaluation of Hazard Potential. *Science and Technology Organization (STO) - Meeting*
574 *Proceedings Paper MP-AVT-272-KN3:1–18*.

575 Clarkson RJ, Simpson H 2017. Maximising Airspace Use During Volcanic Eruptions: Matching
576 Engine Durability against Ash Cloud Occurrence. *Science and Technology Organization*
577 *(STO) - Meeting Proceedings Paper MP-AVT-272-17:1–20*.

578 Clarkson RJ, Majewicz EJE, Mack P 2016. A re-evaluation of the 2010 quantitative
579 understanding of the effects volcanic ash has on gas turbine engines. *Proc. Inst. Mech. Eng.*
580 *G J. Aerosp. Eng.* **230**:2274–2291.

581 Cullen MJP 1993. The unified forecast/climate model. *Met. Mag.* **122**:81–94.

582 Dacre HF, Harvey NJ 2018. Characterising the atmospheric conditions leading to large error
583 growth in volcanic ash cloud forecasts. *Submitted to J. Appl. Meteorol. Climatol.*

584 Dacre HF, Grant ALM, Hogan RJ, Belcher SE, Thomson DJ, Devenish BJ, Marenco F, Hort
585 MC, Haywood JM, Ansmann A, Mattis I, Clarisse L 2011. Evaluating the structure and
586 magnitude of the ash plume during the initial phase of the 2010 Eyjafjallajökull eruption
587 using lidar observations and NAME simulations. *J. Geophys. Res.* **116**:D00U03.

588 Dacre HF, Grant ALM, Johnson BT 2013. Aircraft observations and model simulations of
589 concentration and particle size distribution in the Eyjafjallajökull volcanic ash cloud. *Atmos.*
590 *Chem. Phys.* **13**:1277–1291.

- 591 Dacre HF, Grant ALM, Harvey NJ, Thomson DJ, Webster HN, Marenco F 2015. Volcanic ash
592 layer depth: Processes and mechanisms. *Geophys. Res. Lett.* **42**:637–645.
- 593 Dacre HF, Crawford BR, Charlton-Perez AJ, Lopez-Saldana G, Griffiths GH, Vicencio Veloso J
594 2018. Chilean wildfires: Probabilistic prediction, emergency response and public
595 communication. *B. Am. Meteorol. Soc.* BAMS–D–17–0111.1.
- 596 Devenish BJ, Francis PN, Johnson BT, Sparks RSJ, Thomson DJ 2012. Sensitivity analysis of
597 dispersion modeling of volcanic ash from Eyjafjallajökull in May 2010. *J. Geophys. Res.*
598 *Atmos.* **117**:D00U21.
- 599 Folch A 2012. A review of tephra transport and dispersal models: Evolution, current status, and
600 future perspectives. *J. Volcanol. Geoth. Res.* **235-236**:96–115.
- 601 Gneiting T, Raftery AE 2005. Weather forecasting with ensemble methods. *Science* **310**:248–
602 249.
- 603 Guffanti M, Tupper A 2015. Volcanic Ash Hazards and Aviation Risk. In: *Volcanic Hazards,*
604 *Risks and Disasters*. Elsevier, 87–108.
- 605 Guffanti M, Casadevall TJ, Budding K 2010. Encounters of aircraft with volcanic ash clouds; a
606 compilation of known incidents, 1953-2009. *U.S. Geol. Surv. Data Ser.* **545**:1–16.
- 607 Harvey NJ, Huntley N, Dacre HF, Goldstein M, Thomson D, Webster H 2018. Multi-level
608 emulation of a volcanic ash transport and dispersion model to quantify sensitivity to
609 uncertain parameters. *Nat. Hazards Earth Syst. Sci.* **18**:41–63.
- 610 ICAO 2007. *Doc 9691 AN/954: Manual on Volcanic Ash, Radioactive Material and Toxic*
611 *Chemical Clouds, Second Edition – 2007*. International Civil Aviation Organization:
612 Montréal, Quebec, Canada. <https://skybrary.aero/bookshelf/books/2997.pdf> (accessed 5
613 February 2018).

- 614 ICAO 2016. *Volcanic Ash Contingency Plan, European and North Atlantic Regions. EUR Doc.*
 615 *019, NAT Doc. 006, Part II. Edition 2.0.0 – July 2016.* International Civil Aviation
 616 Organization: Neuilly-sur-Seine, France.
 617 <https://www.icao.int/EURNAT/EUR%20and%20NAT%20Documents/EUR+NAT%20VAC>
 618 [P.pdf](https://www.icao.int/EURNAT/EUR%20and%20NAT%20Documents/EUR+NAT%20VACP.pdf) (accessed 26 February 2018).
- 619 Iman RL, Conover WJ 1980. Small sample sensitivity analysis techniques for computer models,
 620 with an application to risk assessment. *Commun. Stat. Part A* **9**:1749–1842.
- 621 Irvine EA, Hoskins BJ, Shine KP, Lunnon RW, Froemming C 2013. Characterizing North
 622 Atlantic weather patterns for climate-optimal aircraft routing. *Meteorol. Appl.* **20**:80–93.
- 623 Irvine EA, Shine KP, Stringer MA 2016. What are the implications of climate change for trans-
 624 Atlantic aircraft routing and flight time? *Transp. Res. D: Transp. and Environ.* **47**:44–53.
- 625 Jones A, Thomson D, Hort M, Devenish B 2007. The U.K. Met Office's Next-Generation
 626 Atmospheric Dispersion Model, NAME III. In: *Air Pollution Modeling and Its Application*
 627 *XVII*. Boston, MA: Springer US, 580–589.
- 628 Kristiansen NI, Prata AJ, Stohl A 2015. Stratospheric volcanic ash emissions from the 13
 629 February 2014 Kelut eruption. *Geophys. Res. Lett.* **42**:588–596.
- 630 Lawrence BN, Bennett VL, Churchill J, Jukes M, Kershaw P, Oliver P, Pritchard M, Stephens
 631 A 2012. The JASMIN super-data-cluster. *arXiv:1204.3553 [cs.DC]*.
- 632 Lunnon RW, Marklow AD 1992. Optimization of Time Saving in Navigation Through an Area
 633 of Variable Flow. *J. Navig.* **45**:384–399.
- 634 Mastin LG, Guffanti M, Servranckx R, Webley P, Barsotti S, Dean K, Durant A, Ewert JW, Neri
 635 A, Rose WI, Schneider D, Siebert L, Stunder B, Swanson G, Tupper A, Volentik A,
 636 Waythomas CF 2009. A multidisciplinary effort to assign realistic source parameters to

- 637 models of volcanic ash-cloud transport and dispersion during eruptions. *J. Volcanol. Geoth.*
638 *Res.* **186**:10–21.
- 639 Millington SC, Saunders RW, Francis PN, Webster HN 2012. Simulated volcanic ash imagery:
640 A method to compare NAME ash concentration forecasts with SEVIRI imagery for the
641 Eyjafjallajökull eruption in 2010. *J. Geophys. Res. Atmos.* **117**:D00U17.
- 642 Mulder KJ, Lickiss M, Harvey N, Black A, Charlton-Perez A, Dacre H, McCloy R 2017.
643 Visualizing Volcanic Ash Forecasts: Scientist and Stakeholder Decisions Using Different
644 Graphical Representations and Conflicting Forecasts. *Wea. Climate Soc.* **9**:333–348.
- 645 Neal RA, Boyle P, Grahame N, Mylne K, Sharpe M 2014. Ensemble based first guess support
646 towards a risk-based severe weather warning service. *Meteorol. Appl.* **21**:563–577.
- 647 Palmer TN 2002. The economic value of ensemble forecasts as a tool for risk assessment: From
648 days to decades. *Q. J. R. Meteorol. Soc.* **128**:747–774.
- 649 Peterson RA, Dean KG 2007. Forecasting exposure to volcanic ash based on ash dispersion
650 modeling. *J. Volcanol. Geoth. Res.* **170**:230–246.
- 651 Prata AJ, Prata AT 2012. Eyjafjallajökull volcanic ash concentrations determined using Spin
652 Enhanced Visible and Infrared Imager measurements. *J. Geophys. Res. Atmos.* **117**:D00U23.
- 653 Prata AJ, Tupper A 2009. Aviation hazards from volcanoes: The state of the science. *Nat.*
654 *Hazards* **51**:239–244.
- 655 Prata AJ, Kristiansen N, Thomas HE, Stohl A 2018. Ash metrics for European and trans-Atlantic
656 air routes during the Eyjafjallajökull eruption 14 April-23 May, 2010. *J. Geophys. Res.*
657 *Atmos.*

- 658 Rolls-Royce 2017. *All RB211 and Trent Engines - Volcanic Ash Limits Guidance*. Rolls-Royce
 659 plc: Derby, UK. [https://www.wmo.int/aemp/sites/default/files/VA_Limits_Guidance_Rolls-](https://www.wmo.int/aemp/sites/default/files/VA_Limits_Guidance_Rolls-Royce.pdf)
 660 [Royce.pdf](https://www.wmo.int/aemp/sites/default/files/VA_Limits_Guidance_Rolls-Royce.pdf) (accessed 17 November 2017).
- 661 Stohl A, Prata AJ, Eckhardt S, Clarisse L, Durant A, Henne S, Kristiansen NI, Minikin A,
 662 Schumann U, Seibert P, Stebel K, Thomas HE, Thorsteinsson T, Tørseth K, Weinzierl B
 663 2011. Determination of time- and height-resolved volcanic ash emissions and their use for
 664 quantitative ash dispersion modeling: the 2010 Eyjafjallajökull eruption. *Atmos. Chem. Phys.*
 665 **11**:4333–4351.
- 666 Webster HN, Thomson DJ, Johnson BT, Heard IPC, Turnbull K, Marengo F, Kristiansen NI,
 667 Dorsey J, Minikin A, Weinzierl B, Schumann U, Sparks RSJ, Loughlin SC, Hort MC,
 668 Leadbetter SJ, Devenish BJ, Manning AJ, Witham CS, Haywood JM, Golding BW 2012.
 669 Operational prediction of ash concentrations in the distal volcanic cloud from the 2010
 670 Eyjafjallajökull eruption. *J. Geophys. Res. Atmos.* **117**:D00U08.
- 671 Witham CS, Webster HN, Hort MC, Jones A, Thomson D 2012. Modelling concentrations of
 672 volcanic ash encountered by aircraft in past eruptions. *Atmos. Environ.* **48**:219–229.
- 673 Witham CS, Hort MC, Thomson D, Leadbetter SJ, Devenish BJ, Webster HN, Beckett FM 2016.
 674 The current volcanic ash modelling set-up at the London VAAC. *Met Office Technical*
 675 *Summary (v1.3)*:1–9.
- 676 Wylie S, Bucknell A, Forsyth P, McGilvray M, Gillespie DRH 2017. Reduction in Flow
 677 Parameter Resulting From Volcanic Ash Deposition in Engine Representative Cooling
 678 Passages. *J. Turbomach.* **139**:031008.

689

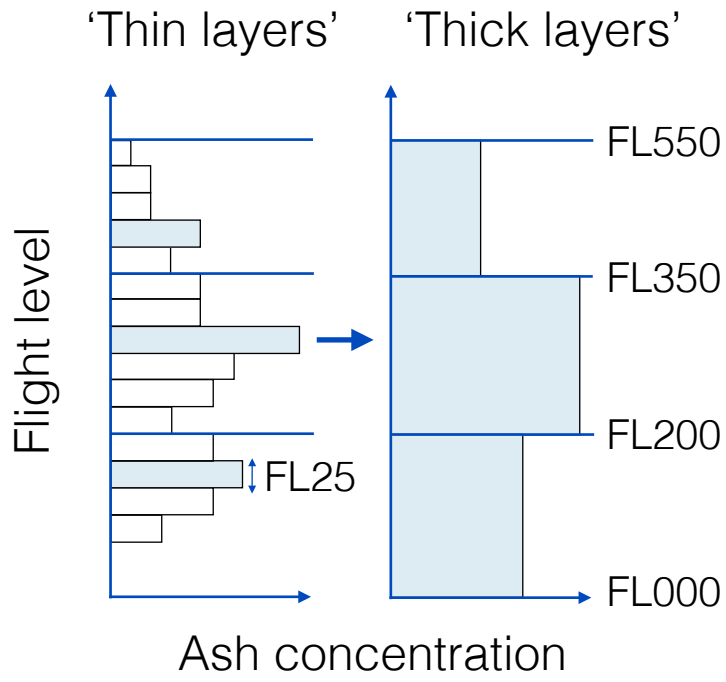
681 **Tables**

Parameter	Control value	Sampling range
Plume height (km)	15	13 to 17
Mass eruption rate factor	1	1/3 to 3
Source duration (h)	16	6 to 26
Source timing (UTC)	0300 1 Jan 2017	0300 to 1300 1 Jan 2017
Distal fine ash fraction (%)	5	1 to 10
Horizontal (vertical) Lagrangian timescale (τ) for free tropospheric turbulence (s)	300 (100)	100 to 900 (33.33 to 300)
Standard deviation (σ) of horizontal (vertical) velocity for free tropospheric turbulence (m s^{-1})	0.25 (0.10)	0.0025 to 2.5 (0.001 to 1)
Standard deviation (σ) of horizontal velocity for unresolved mesoscale motions (m s^{-1})	0.8	0.27 to 1.74
Meteorological fields	MetUM analysis	ECMWF members 0 to 19

682 Table 1. Control run parameters selected for Latin Hypercube Sampling.

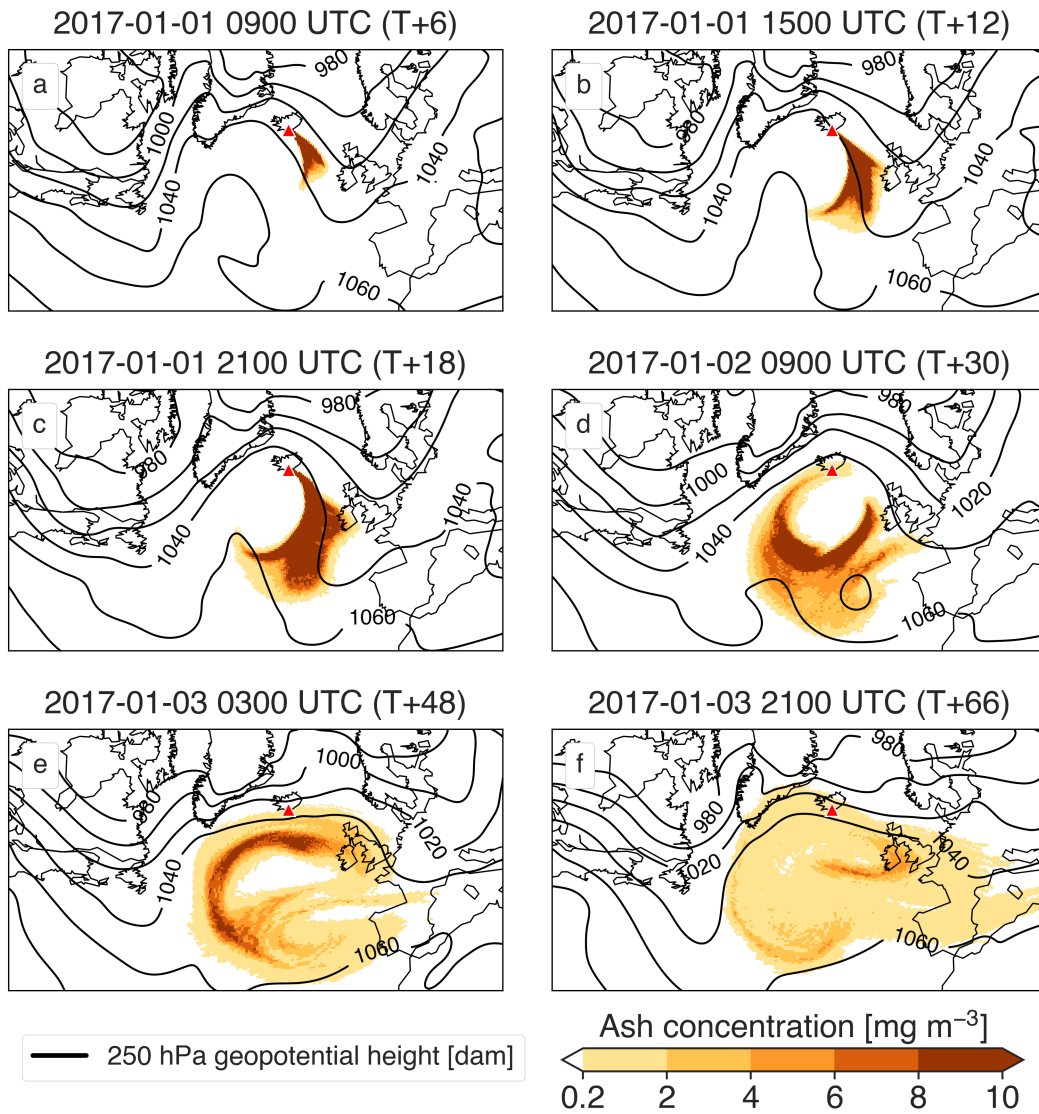
683

684 **Figures**



685

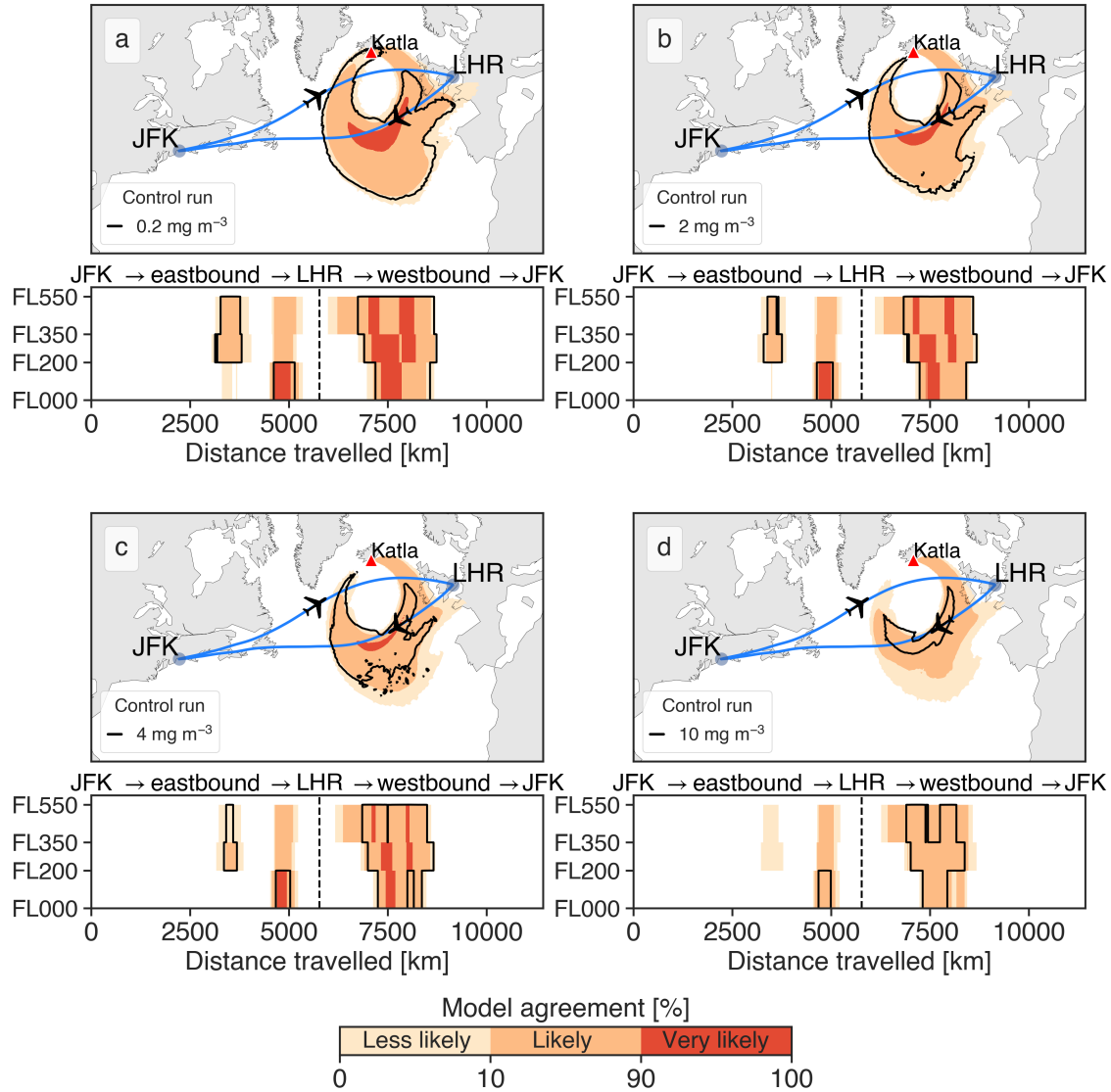
686 Figure 1. Schematic showing the difference between the thin layer and thick layer LVAAC setup of NAME.



687

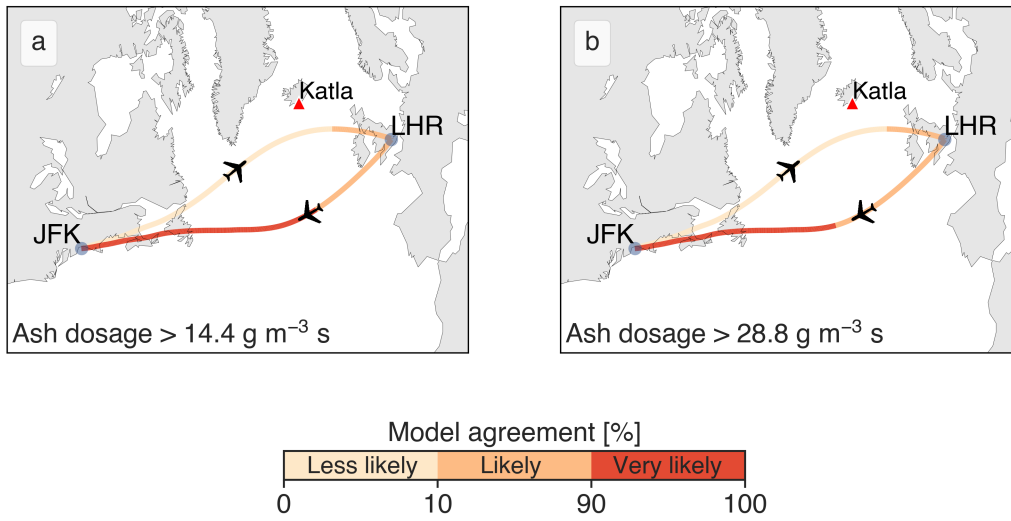
688 Figure 2. Ash concentrations for the control run simulation for the Katla (indicated by the red triangle) eruption
 689 scenario with 250 hPa geopotential height contours overlaid. The control run start time is 0300 UTC on 1 January
 690 2017. Concentrations have been post-processed to produce the LVAAC's thick layer product from FL350–FL550.
 691 (a) 6, (b) 12, (c) 18, (d) 30, (e) 48, (f) 66 hours after eruption.

Volcanic ash dosage and concentration risk



692

693 Figure 3. Percentage of ensemble members at T+30 that resulted in ash concentrations above (a) 0.2 mg m⁻³, (b) 2
 694 mg m⁻³, (c) 4 mg m⁻³ and (d) 10 mg m⁻³. Each panel shows the geographic model agreement and the relevant ash
 695 concentration contour for the control run (black line) at the FL350–FL550 thick layer level (top) and the vertical
 696 cross-section of model agreement and the relevant ash concentration contour along the JFK–LHR and LHR–JFK
 697 time-optimal routes (bottom).



698

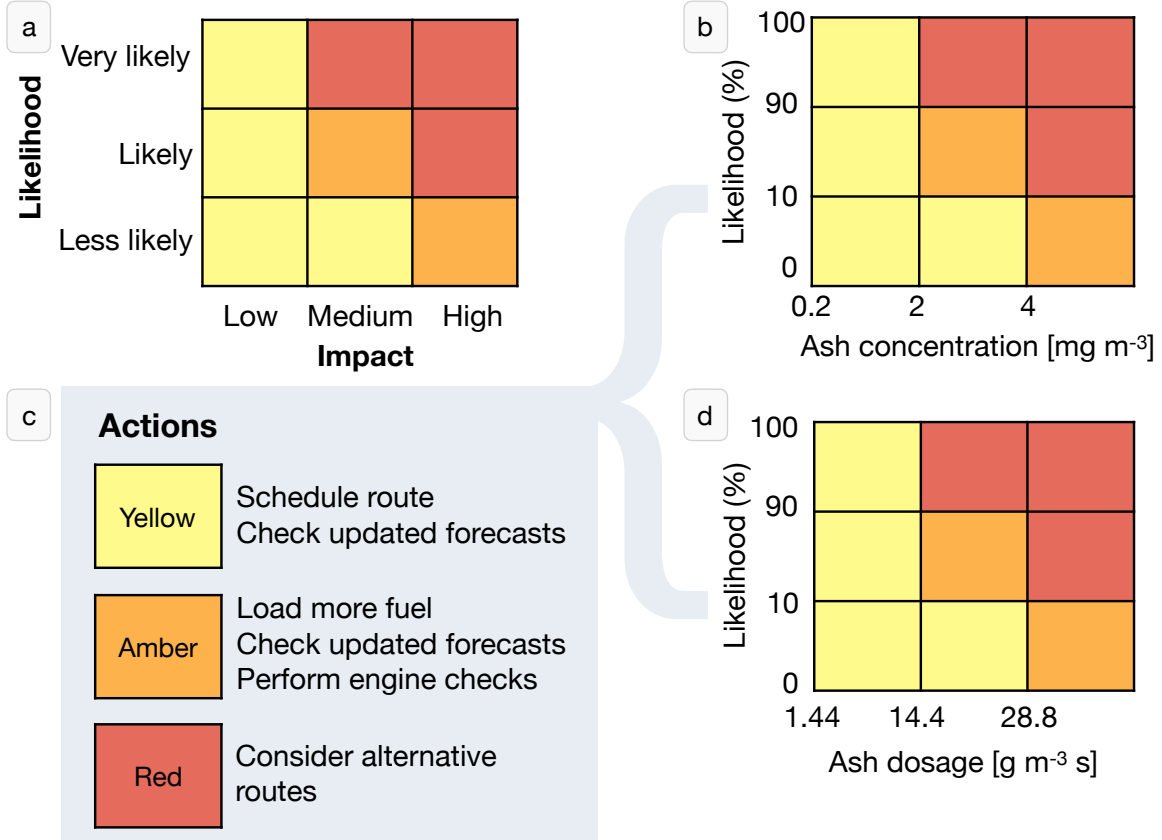
699 Figure 4. Percentage of ensemble members that resulted in ash dosages above (a) 14.4 g m⁻³ s and (b) 28.8 g m⁻³ s.

700 Percentages have been calculated along the time-optimal eastbound and westbound flight routes between JFK and

701 LHR at T+30 for the FL350-FL550 thick layer level.

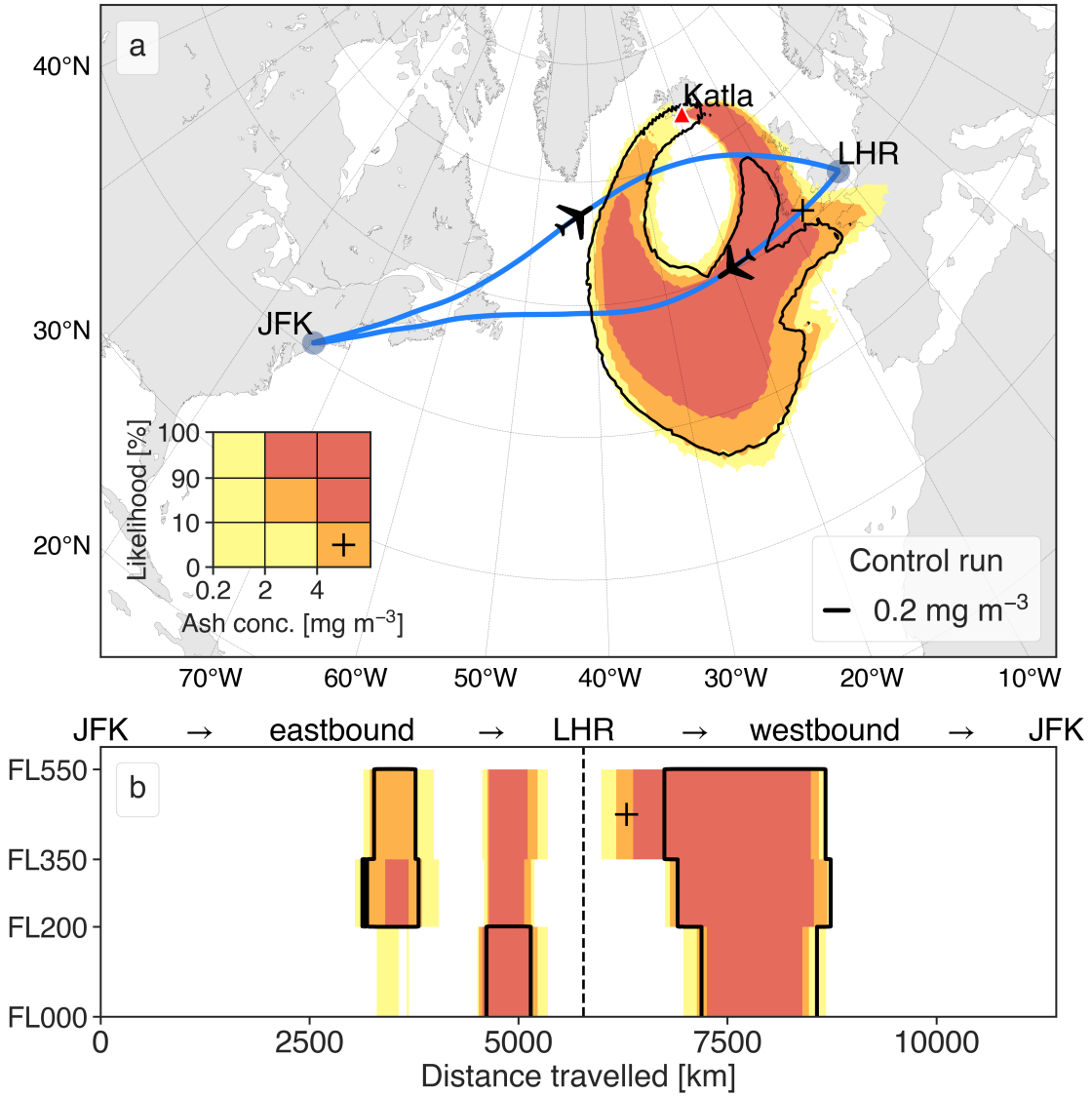
702

Risk = Impact x Likelihood



703

704 Figure 5. Schematic showing (a) a generic risk matrix, (b) how the ash concentration risk matrix was constructed, (c)
 705 example actions that could be taken by a decision-maker in response to a yellow, amber or red warning and (d) how
 706 the ash dosage risk matrix was constructed.



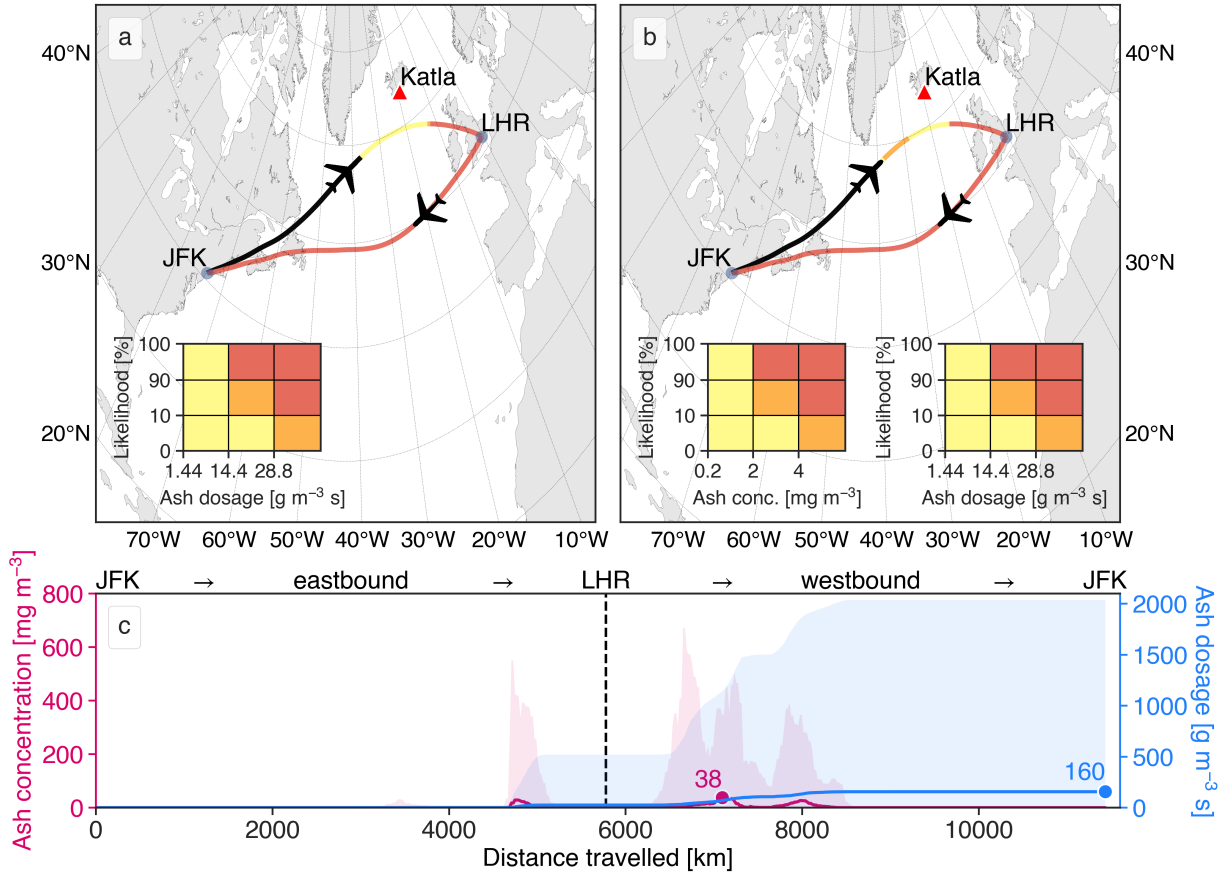
707

708 Figure 6. (a) Horizontal ash concentration risk map for the thick layer level (FL350–FL550) at T+30. (b) Vertical

709 risk maps for each thick layer corresponding to the return JFK–LHR route (plotted on (a)) at T+30. The ‘+’

710 annotated on the risk matrix (inset of (a)) corresponds to the risk level at the location of the ‘+’ on (a) and (b).

Volcanic ash dosage and concentration risk



711

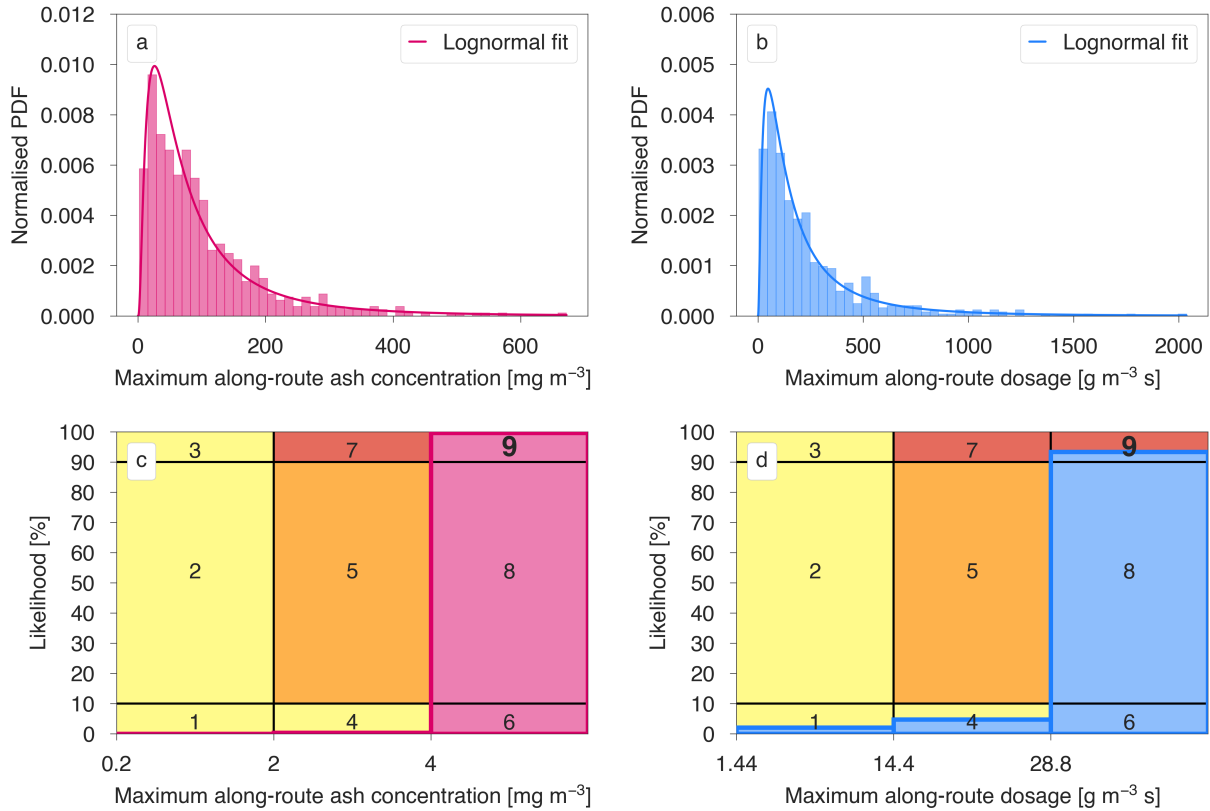
712 Figure 7. (a) Dosage risk for the New York (JFK) to London (LHR) trans-Atlantic air-route at T+30 and thick layer

713 level FL350–FL550. (b) Dosage and ash concentration risk for the same route in (a). (c) Along-route ash

714 concentration and dosage. Values annotated are the ensemble median maximum values correct to two significant

715 figures; shaded regions correspond to minimum and maximum of the ash concentration and dosage.

716



717

718 Figure 8. Normalised probability density functions (PDFs) of the maxima of the (a) along-route ash concentration
 719 and (b) along-route dosage for the return air-route from New York (JFK) to London (LHR) at T+30 and thick layer
 720 level FL350–FL550 (lines plotted over each histogram indicate a Lognormal distribution fit). The ‘risk PDFs’
 721 corresponding to the distributions shown in (a) and (b) are illustrated in (c) and (d), respectively. Note that the
 722 numerical values annotated on (c) and (d) indicate the risk level, with the risk issued shown in bold). The pink and
 723 blue histograms plotted over the risk matrix have been re-binned according to the impact boundaries shown in
 724 Figure 5.